The Astronomical Journal, 143:84 (10pp), 2012 April doi:10.1088/0004-6256/143/4/84

EIGHT HUNDRED NEW CANDIDATES FOR GLOBULAR CLUSTERS IN NGC 5128 (Centaurus A)*

Gretchen L. H. Harris[1], Matías Gómez[2], William E. Harris[3], Kyle Johnston[1], Farnoud Kazemzadeh[1],
Wolfgang Kerzendorf[4], Doug Geisler[5], and Kristin A. Woodley[6]
[1] Department of Physics and Astronomy, University of Waterloo, Waterloo, ON, Canada; glharris@astro.uwaterloo.ca,
kyjohnston@rim.com, farnoud.kazemzadeh@gmail.com
[2] Departamento de Ciencias Fisicas, Facultad de Ciencias Exactas, Universidad Andres Bello, Santiago, Chile; matiasgomez@unab.cl
[3] Department of Physics and Astronomy, McMaster University, Hamilton, ON L8S 4M1, Canada; harris@physics.mcmaster.ca
[4] Mount Stromlo Observatory, The Research School of Astronomy and Astrophysics, Australian National University,
Weston Creek, ACT 2611, Australia; wkerzend@mso.anu.edu.au
[5] Departamento de Astronomía, Universidad de Concepción, Chile; dgeisler@astro-udec.cl
[6] Department of Physics and Astronomy, University of British Columbia, Vancouver, BC V6T 1Z1, Canada; kwoodley@phas.ubc.ca

Received 2011 July 29; accepted 2012 January 16; published 2012 March 9

ABSTRACT

We have used new wide-field imaging with the Magellan IMACS camera to search for globular cluster (GC) candidates around NGC 5128, the nearest giant E galaxy. The imaging data are in the *B* and *R* broadband filters and cover a 1.55 deg^2 field centered on the galaxy, corresponding to an area about 90×90 kpc^2 at the distance of NGC 5128. All the fields were taken under exceptionally high-quality seeing conditions (FWHM $= 0\farcs4$–$0\farcs5$ in *R*). Using this material we are able, for the first time in the literature, to construct a homogeneous list of GC candidates covering a wide span of the NGC 5128 halo and unusually free of field contaminants (foreground stars and faint background galaxies). Selecting the measured objects by color, magnitude, ellipticity, and profile size gives us a final catalog of 833 new high-quality GC candidates brighter than $R = 21$ (0.8 mag fainter than the standard GC luminosity function turnover point). The measured positions have better than $0\farcs2$ precision in both coordinates. This list can be used as the basis for spectroscopic follow-up, leading to a more comprehensive kinematic and dynamic study of the halo.

Key words: galaxies: elliptical and lenticular, cD – galaxies: individual (NGC 5128) – galaxies: star clusters: general – globular clusters: general

Online-only material: color figures, machine-readable and VO table

1. INTRODUCTION

Globular clusters (GCs), the massive, compact remnants of early star-forming phases in the history of galaxies, have continually proved to be effective tracers of those first eras in a wide variety of directions (see, e.g., Harris 1991, 2010b; Ashman & Zepf 1998; Brodie & Strader 2006 for recent reviews). Two of their most important attributes are that they can be found and individually measured in galaxies well beyond the Local Group, and also that big galaxies may host large numbers of GCs (many thousands in the case of the giant ellipticals). Because to first order each individual GC has a single age and abundance, it is then possible to construct metallicity and age distribution functions for them with useful statistical weight.

NGC 5128 (also widely known as Centaurus A, after its luminous central radio source) is the nearest easily observable giant elliptical galaxy, and the dominant central member of the nearby Centaurus group at a distance of 3.8 ± 0.1 Mpc (Harris 2010a; Harris et al. 2010a). As such, it has long provided a unique opportunity to study an entire system of GCs in a gE galaxy at close range and at a level of detail that is not possible for any other galaxy of this type (the next nearest such GC populations—in the Leo group elliptical NGC 3379 at 10 Mpc, and the Virgo giants at 16 Mpc—are more than 2 mag fainter). For these reasons, finding and measuring the NGC 5128 clusters has been well worth the effort, leading to a range of conclusions about its formation history (Peng et al. 2004a; Woodley et al. 2010a, 2010b; Woodley & Harris 2011).

Identifying the NGC 5128 GC population is, however, made more difficult on strictly observational grounds because its proximity means that its halo is spread out across the sky, diluting the GC population against the field of both foreground stars and faint background galaxies. Because NGC 5128 is also at intermediate galactic latitude ($b = 19°$), there are large numbers of *both* types of field contaminants present. The only definitive ways to identify its GCs one by one are as follows.

1. *Direct resolution of the GC into stars*. This method can so far be done effectively only by the *Hubble Space Telescope* (*HST*) cameras (Harris et al. 1998, 2002, 2006; Mouhcine et al. 2010) and the observation time is costly. Nevertheless, some dozens of GCs, including most of the faintest known ones, have been identified this way.
2. *Radial velocity measurement*. Because the systemic velocity of the galaxy is $\simeq$540 km s^{-1} and the velocity dispersion of the GC system is $\simeq$160 km s^{-1} (Woodley et al. 2010a), all background galaxies can be eliminated by velocity measurement, as well as all Milky Way foreground stars except a thinly populated overlap region around ∼150–250 km s^{-1} that includes some Milky Way halo stars. Velocity measurements have the additional powerful benefit of providing the raw material for a kinematic and dynamic analysis of the host galaxy's halo, with its direct connections to the dark-matter distribution and the evolutionary history of the oldest parts of the galaxy including remnants of satellite accretion (Peng et al. 2004a; Woodley et al. 2010a, 2010b; Woodley & Harris 2011).

To date, 607 GCs in NGC 5128 have been identified by combinations of these methods (see Woodley et al. 2007, 2010a

---

[*] This Paper includes data gathered with the 6.5 m Magellan Telescopes located at Las Campanas Observatory, Chile.

for the catalog of 605 clusters; two other very faint ones found serendipitously in a deep *HST* field have been added by Mouhcine et al. 2010). These, however, are likely to represent only about half the total population (Harris et al. 2004b, 2006; Harris 2010a). In particular, the numbers of known GCs in the outer halo beyond $R_{\rm gc} \gtrsim 25$ kpc and along the minor axis are worrisomely incomplete, leading to possible biases in the kinematic and dynamic solutions (Woodley et al. 2007, 2010a). In these outer regions the numbers of clusters are smallest and the relative effects of field contamination worst.

Beginning with the discovery of the very first GC by Graham & Phillips (1980), early photometric and spectroscopic work led to the slow, painstaking identification of roughly 80 GCs and a first assessment of the properties of the system as a whole (van den Bergh et al. 1981; Hesser et al. 1984, 1986; Harris et al. 1992). A second major step forward that took advantage of the newer wide-field CCD cameras was completed by Peng et al. (2004a, 2004b), who identified 138 new clusters spectroscopically and also measured integrated colors. A third major cycle of spectroscopic work relying heavily on multi-object spectroscopy from several telescopes (Woodley et al. 2005, 2007, 2010a, 2010b; Beasley et al. 2008) has tripled the identified population and built the list of 607 GCs as it now stands.

Further major progress in isolating more GCs in this uniquely valuable galaxy becomes progressively more difficult. The essential nature of the problem is that across the $\gtrsim 2^\circ$ span of the NGC 5128 halo on the sky, there are only $\sim$1500 GCs hiding among several hundred thousand field stars and galaxies over the same magnitude range (Harris et al. 2004a; Harris 2010a), so in raw terms the "signal-to-noise ratio" (S/N) is less than 1:100. It has long been realized that the fastest way to weed out most of the contaminants is to use the empirical fact that with *high-resolution imaging*, the GCs become visibly nonstellar in morphology and their profile structures are resolved. A typical GC half-light diameter of 5 pc (e.g., Harris 2009) corresponds to $\simeq 0\farcs3$ at the distance of NGC 5128, which is enough to be clearly detectable and measurable with sub-arcsecond ground-based seeing (see Rejkuba et al. 2001; Gómez et al. 2006; Gómez & Woodley 2007 for such work). If the imaging is good enough, virtually all the foreground stars in the field can be eliminated and the only remaining contaminants are faint, small background galaxies. Adding other criteria such as color and morphology can then restrict the list further, as will be seen below.

Acquiring the right imaging material with modern wide-field CCD array cameras has, however, been remarkably difficult. Previous wide-field surveys (Peng et al. 2004b; Harris et al. 2004a, 2004b) were taken under seeing conditions of $1''$–$2''$ that made them unable to distinguish a high fraction of the clusters from stars. Conversely, the sub-arcsecond imaging work previously done at different places in the halo was restricted to much smaller fields (Rejkuba et al. 2001; Gómez et al. 2006; Holland et al. 1999; Harris et al. 1998, 2002, 2006).

In this Paper, we describe the results from an unusually high-quality imaging data set that allows us to combine the advantages of wide field and high resolution in a new search for NGC 5128 clusters. Our final result of more than 800 new cluster candidates can be used as the basis for follow-up spectroscopic work.

In the following discussion, we adopt for NGC 5128 an intrinsic distance modulus $(m - M)_0 = 27.90$ and foreground reddening $E_{B-V} = 0.11$ (Harris et al. 2010a).

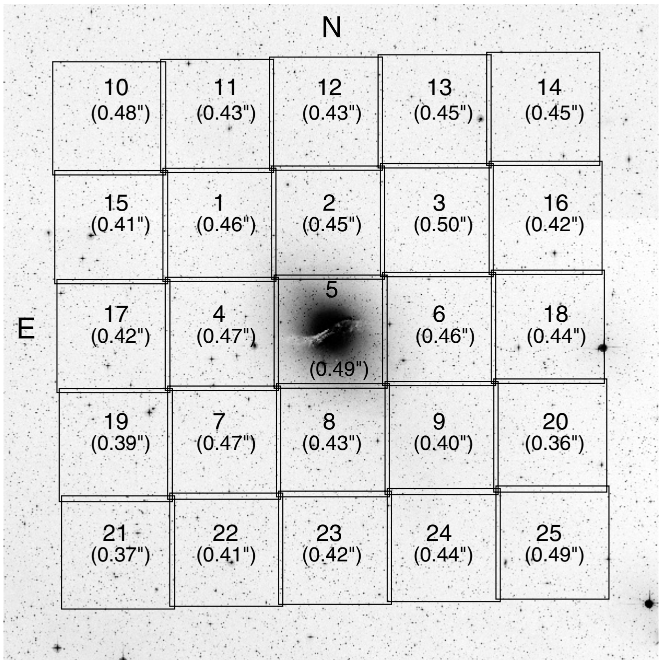

Figure 1. Layout of the IMACS target fields centered on NGC 5128, shown on a Digital Sky Survey image of the region centered on the galaxy. Each square is $15' \times 15'$ and the entire array covers $1\fdg2 \times 1\fdg2$. Target pointings 1 through 9 are the central 3 × 3 array while 10 through 25 are the "outer ring." As described in the text, R-band exposures were taken for all 25 fields, while B-band exposures were taken for only the outer ring. The mean seeing quality of the R-band images (FWHM) is labeled inside each square.

2. OBSERVATIONS AND DATA REDUCTION

During the night of 2006 April 7, we used the Inamori Magellan Areal Camera and Spectrograph (IMACS) camera at the Magellan Observatory Baade telescope, under unusually good and steady seeing conditions, to image a wide area centered on NGC 5128. The camera provides a mosaic of 4 × 2 CCDs (each of dimension 2048 × 4096 pixels) making a single square field of $15\farcm4 \times 15\farcm4$ per exposure. The image scale is $0\farcs111$ pixel^{-1}, the CCD gain $0.9e^-$/adu, and the readnoise $4.9e^-$ rms. Images were taken in standard broadband filters B and R, each with "long" (300 s) and "short" (30 s) exposure times.

In the R band, a total of 25 target fields were imaged, in a 5 × 5 matrix centered on NGC 5128. The total set of R images thus provides complete coverage of a 1.4 deg^2 area centered on the galaxy. These pointings are illustrated in Figure 1. Slight overlaps between pointings were used to check the internal consistency of the photometric calibrations and the candidate identification discussed below. In the B band, the available observing time did not permit covering this entire area, but we obtained blue exposures for the outer ring (fields 10–25 in Figure 1). For the purposes of two-color photometry, the inner 3 × 3 region is already completely covered by our earlier work with the CTIO BTC camera (Big Throughput Camera; Harris et al. 2004a, 2004b).

The key to the present analysis was the seeing quality particularly on the R-band images, which averaged $<0\farcs5$ with only small differences between fields (see Figure 1 for the mean FWHM on the R frames for each field). This level is similar to what we achieved in an earlier study at Magellan (Gómez et al. 2006) with the MagIC camera (which had a field of view $2\farcm36 \times 2\farcm36$, thus 42 times smaller area than the IMACS). The

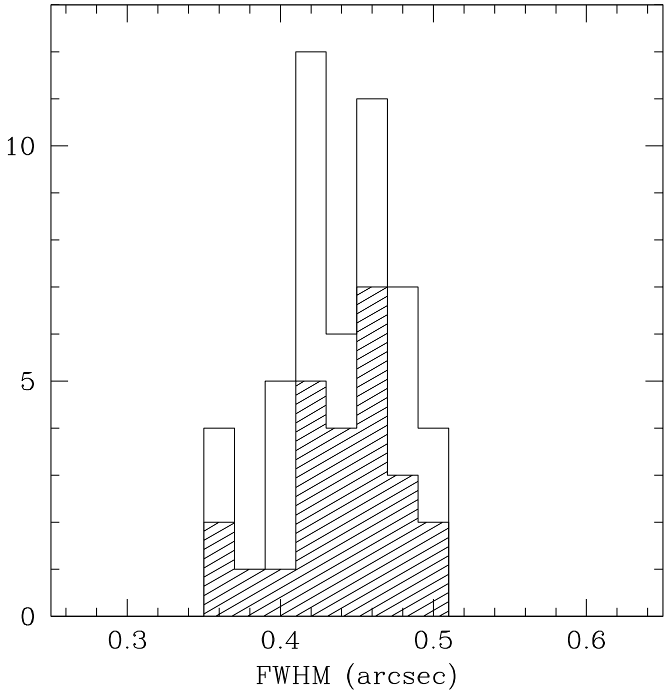

Figure 2. Distribution of the FWHM of point-spread functions (PSFs) for the *R*-band images in our study. The shaded histogram shows the distribution for the short (30 s) exposures, and the unshaded histogram for the long (300 s) exposures.

distribution of measured seeing FWHMs for the *R* images that were primarily used to identify candidates (see below) is also shown in Figure 2. The measured FWHMs ranged from $0''.35$ to $0''.50$ with an average of $0''.45$. This single characteristic enabled us to carry out a homogeneous detection of cluster candidates over the entire $1^{\circ}.2 \times 1^{\circ}.2$ survey area. The seeing quality was not quite as good on the *B* images (typically $0''.7$), but these images were used primarily for later measurement of color indices and not for raw identification of the GC candidates.

2.1. Candidate Identification

The first stage in the analysis was, in descriptive terms, to search for small, slightly nonstellar objects. In this step no attention was paid to the object's magnitude, color, shape, or whether it was already known to be a GC. The single exception to this statement was that we ignored obvious small background galaxies (such as with spiral arms, disks, asymmetric blobs, companions, etc.).

This first stage was similar to the technique used in several other previous studies (e.g., Rejkuba et al. 2001; Harris et al. 2004b; Gómez et al. 2006) and is also illustrated here in Figure 3. We carried out *iraf/daophot/allstar* point-spread function (PSF) fitting photometry for all the images in the short- and long-*R* exposures, including the normal sequence of finding all objects above a specified threshold (*daofind*), aperture photometry (*phot*), construction of a PSF for each CCD in each field (*pstselect, psf*), and fitting the PSF to all objects (*allstar*). These steps generated a "subtracted" image of each field in which the genuine stars are cleanly removed, while any nonstellar objects remain present as doughnut-shaped ellipses with oversubtracted cores and undersubtracted wings (see, e.g., Rejkuba et al. 2001; Gómez et al. 2006 for sample illustrations). Blinking the subtracted image with the original image allows

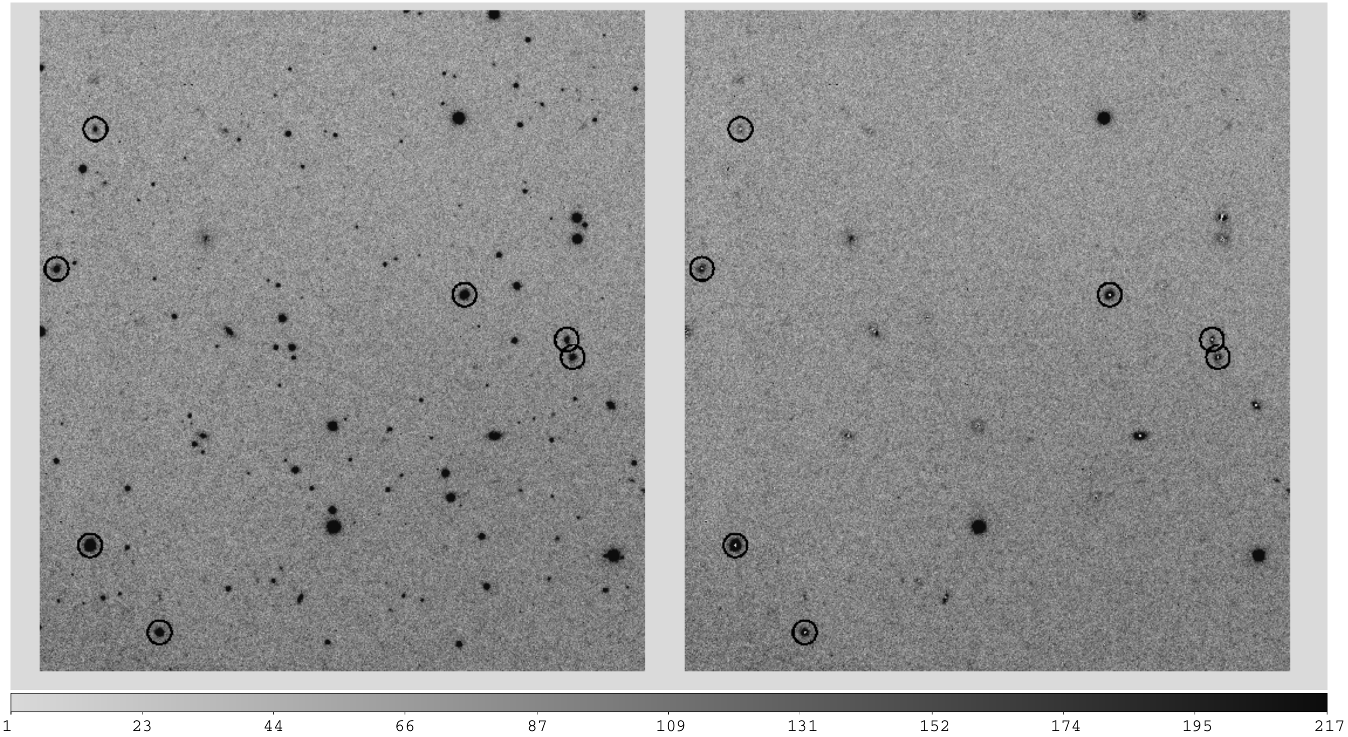

Figure 3. Visual example of the PSF-subtraction technique described in the text. Left panel: a $2'.3$ wide portion of the "long-*R*" exposure in field 1. Note the wide mixture of foreground stars and faint background galaxies. Seven globular cluster candidates identified in our procedure are circled; the brightest three of these were previously known to be GCs. Right panel: the same field, after the *daophot/substar* step that subtracts out the PSF fits to all the detected objects. The GC candidates show up as nonstellar objects with oversubtracted cores and undersubtracted wings. A few strongly elliptical or asymmetric objects were categorized as galaxies and not selected. Note in this panel the "clean" subtraction of the stars, which greatly outnumber the clusters; note also three bright stars that were partially saturated and thus not PSF-fitted.

these doughnut-shaped residual objects to be easily identified and marked. Two of us (G.L.H.H., W.E.H.) did this scanning identification independently for all the short and long-*R* frames, and the resulting lists were combined.

In each CCD chip, the PSF was defined from the average of dozens to hundreds of starlike objects (which dominate the population of the brightest objects in each field). By rigorously presetting the expected FWHM of the PSF in the *daophot/psf* step, almost all nonstellar objects could be rejected from PSF candidate lists. A sensitive test of whether the PSF is significantly contaminated by galaxies or clusters (and thus too broad) appears in the PSF-subtracted images, where ideally the star images will all be cleanly subtracted with no residuals. Figure 3, drawn from field 1, is one representative example. We have found no evidence that the PSF structure is biased away from stellar in any of our fields. The key feature of the data that facilitated this step is the same one mentioned above, that stars outnumber GCs (or candidates) by a very large factor everywhere in the region.

Figure 3 also illustrates the typical degree of *crowding* across our fields, which is quite low. Even in the innermost field 5, valid PSF subtraction and aperture photometry was straightforward. In addition, to within $\pm 0\farcs05$ we found no detectable difference in PSF size or shape to well within $\pm 0\farcs05$ between the eight CCDs in each field. Any such trends were smaller than the already-small differences in seeing between pointings during the night (Figure 2) and thus had no important effect on our ability to find GC candidates as a function of location. As will be described below, the final *selection* threshold magnitude was placed much brighter than the object *detection* threshold, so all the candidates in the final list had high S/N.

In parallel, we carried out measurements of all the frames with SourceExtractor (SE; Bertin & Arnouts 1996) and used its resulting object size measurements (specifically the FWHM value; see our later discussion below) to identify clearly nonstellar ones. These lists correlated very well with our PSF-subtracted scans described above. The agreement was particularly complete for the high-S/N magnitude range $R < 21$ which, as will be seen below, defines the useful limit of our data that was ultimately set by field contamination.

The effective limiting magnitude of our initial detections is set by the long-*R* exposures and is much fainter than $R = 22$ (see the color/magnitude photometric results below). This level lies well below the classic GC luminosity function "turnover point" at $M_V = -7.4$, $M_R = -7.9$ (Harris 1991) which corresponds to $R \simeq 20.2$ for NGC 5128. However, our final list included only objects that could be measured in both *B* and *R*, and because the *B*-band images did not reach as faint, they set the photometric limit of our candidate list, which is at $R \simeq 22$. In principle, our data should then include up to ≃90% of the total cluster population. As will be seen below, however, fainter than $R \simeq 21$ the field contamination becomes overwhelmingly large and in the end this factor—not the raw photometric limit—is what sets the useful practical limit of our survey. Said another way, we could identify candidate nonstellar objects with high completeness to a far fainter level than eventually proved to be useful for the study.

The other type of limit relevant to our data is one of spatial resolution. Extensive tests on similar data with simulated cluster profiles (Larsen 1999; Harris 2009; Harris et al. 2009) show that for objects with well-exposed images clearly above the photometric limit, nonstellar objects can be reliably distinguished from stars down to a level FWHM(GC) ≃ 0.2 FWHM(PSF). For NGC 5128 and a seeing FWHM of $0\farcs5$ this threshold corresponds to a linear size FWHM(GC) ≃ 1.8 pc. This level is well below the 5–6 pc diameter of typical GCs, although the most compact normal GCs have half-light diameters near 2.0 pc (Harris et al. 2010b), which is near the predicted resolution threshold. For comparison, Gómez & Woodley (2007) successfully measured linear sizes on these IMACS images down to a lower limit of 2 pc diameter; in addition, Gómez et al. (2006) found typical measurement precisions in cluster half-light *radius* $r_{\rm h}$ of ±0.9 pc, from Magellan/MagIC-camera images of 39 individual clusters with similar exposure times and seeing levels to our IMACS data. These results are consistent with our predicted size thresholds.

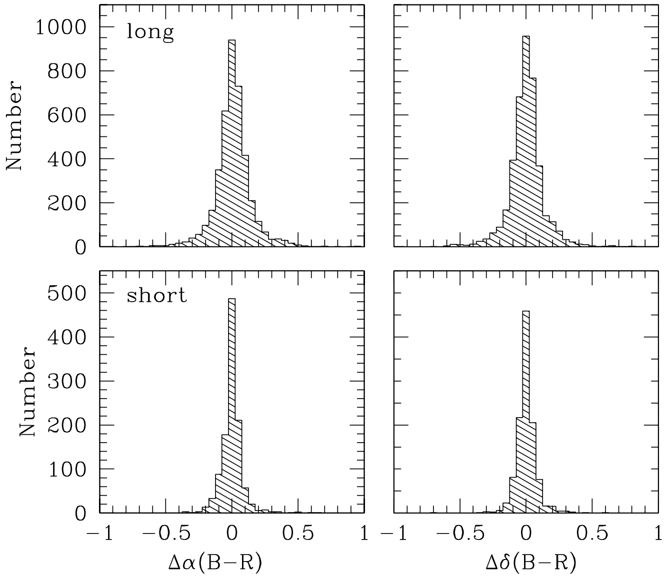

Figure 4. Comparison of coordinates measured in the present study between the *B* and *R* images. The two upper panels show the difference between the 300 s exposures in right ascension (left) and declination (right), while the lower panels show the difference between the 30 s exposures. Horizontal axis is in units of arcseconds.

In summary, we expect a small fraction of the cluster population—the very most compact ones—to be missed by our IMACS survey, but the great majority of the GC size distribution is successfully captured. To quantify our nonstellar candidates and the resolution limits further, we are carrying out more extensive profile-fitting work and will present this in a later paper.

2.2. Astrometry

Astrometry was performed for each target field (both *B* and *R*) and independently for each CCD in the IMACS array. The solutions were calculated with *astrometry.net* (Lang et al. 2010) and the USNO-B catalog (Monet et al. 2003) was used as an astrometric reference for the astrometry-solver. We adopted the gnomonic projection for further work (Calabretta & Greisen 2002).

The internal precisions of the coordinates can be estimated by intercomparison of the independent *B* and *R* frames. These are shown in Figure 4.[7] Comparing the long exposures, we find mean differences and standard deviations (in the sense

---

[7] This comparison can be done only for the 16 outer-ring IMACS fields, since as noted above, no *B* exposures were taken for the inner nine fields.

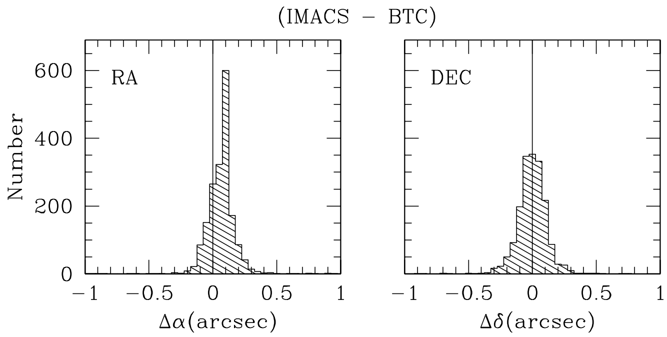

Figure 5. Comparison of coordinates measured in the present study vs. data from the BTC catalog of Harris et al. (2004a).

B minus R):

$$\Delta\alpha = 0\farcs059, \quad \Delta\delta = 0\farcs011,$$

$$\sigma(\alpha) = 0\farcs098, \quad \sigma(\delta) = 0\farcs103.$$

For the short exposures we find

$$\Delta\alpha = 0\farcs001, \quad \Delta\delta = -0\farcs001,$$

$$\sigma(\alpha) = 0\farcs079, \quad \sigma(\delta) = 0\farcs077.$$

We find no indication that these parameters change significantly from one part of the survey field to another. The mean difference between the long-and short-R exposures is well within ±$0\farcs1$. To generate our final candidate coordinates, we averaged the short-R and long-R exposures since these had higher S/N than the equivalent B exposures, and they covered all 25 survey fields.

To further gauge the accuracy of the IMACS coordinates, we also match objects in our list with those from the CTIO/BTC catalog (Harris et al. 2004a) which covers nearly the same area although at much poorer seeing quality. We find (in the sense (IMACS-BTC))

$$\Delta\alpha = 0\farcs064, \quad \Delta\delta = 0\farcs000,$$

$$\sigma(\alpha) = 0\farcs157, \quad \sigma(\delta) = 0\farcs162.$$

These are displayed in Figure 5. As described in detail in Harris et al. (2004a), the BTC coordinates were reduced to the USNO UCAC2 catalog. A slight offset in right ascension between the two systems appears to exist, equivalent to about half an IMACS pixel; otherwise, the comparisons confirm internal uncertainties near ±$0\farcs16$ for both axes.

Finally, we compare the IMACS astrometry with the previously published catalog positions for the known GCs, taken from Woodley et al. (2007, 2010b). By cross-identifying the lists we have recovered 458 (75%) of the 607 known clusters to within a matching radius of $1\farcs5$. The remaining 149 not recovered are mostly objects along the inner dust lane or in the bright central bulge where their initial identification in the subtracted-image scans was more difficult; or objects falling in the CCD chip gaps; or else fainter ones past the reliable limits of the IMACS images. For the 458 recovered clusters, we find (IMACS-catalog) differences

$$\Delta\alpha = 0\farcs041, \quad \Delta\delta = -0\farcs005,$$

$$\sigma(\alpha) = 0\farcs156, \quad \sigma(\delta) = 0\farcs135.$$

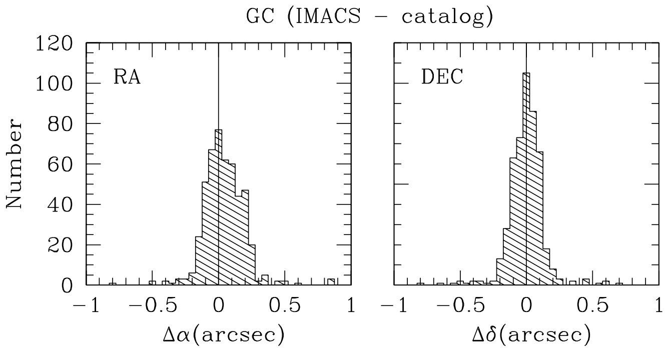

Figure 6. Comparison of coordinates measured in the present study for the previously known globular clusters vs. data from the NGC 5128 cluster catalog (Woodley et al. 2007, 2010a).

These are displayed in Figure 6. In our BTC database discussion (Harris et al. 2004a) more extensive comparisons with earlier GC survey papers were presented and will not be repeated here. The new IMACS reduction, drawing on a superior camera and calibrations, reduces the uncertainties to levels approaching ±$0\farcs15$ rms in both α and δ.

2.3. Photometry

Magnitudes for all the candidates were measured with simple concentric-aperture photometry through the same *iraf/daophot* procedures initially used to find nonstellar objects. A standard aperture diameter of 20 pixels ($2\farcs2$) was used for all objects to define instrumental magnitudes b_{ap} and r_{ap}. Although the individual objects have slightly different linear sizes, this diameter was large enough (40 pc at the distance of NGC 5128) to include most of the light of real GCs. Our goal in this study was simply to generate a catalog of GC candidates with preliminary values of magnitudes and colors useful for planning follow-up spectroscopic work and more detailed profile measurement.

During the observing run, a small number of standard star fields were imaged, but the weather was not consistently photometric and these few proved to be insufficient for calibration of the zero points to the desired accuracy. To make a first estimate of the magnitude scales, we therefore used the Washington photometry from our previous BTC study (Harris et al. 2004a) along with the transformations given by Geisler (1996),

$$B = C + 0.128 - 0.269(C - T_1),$$

$$R = T_1 + 0.003 - 0.017(C - T_1).$$

We then cross-identified objects in the BTC catalog with our new list of GC candidates, finding 2300 objects in common. For these we converted (C, T_1) to predicted values of (B, R) and then calculated the mean $\langle B - b_{\mathrm{ap}}\rangle$, $\langle R - r_{\mathrm{ap}}\rangle$ where as noted above, the aperture magnitudes were those measured through a 20 pixel diameter. These mean zero points were used wholesale to convert the instrumental $b_{\mathrm{ap}}, r_{\mathrm{ap}}$ magnitudes into first estimates of B, R for the entire candidate list.

Although these zero points bring the photometry close to the true B, R scales, their expected accuracy is no better than ±0.1 mag because of the combined uncertainties in transforming between filter systems, and in the Washington BTC catalog magnitudes themselves (see Harris et al. 2004a for detailed discussion). As a final step, we therefore used the magnitudes for the GCs studied by Peng et al. (2004b), which were

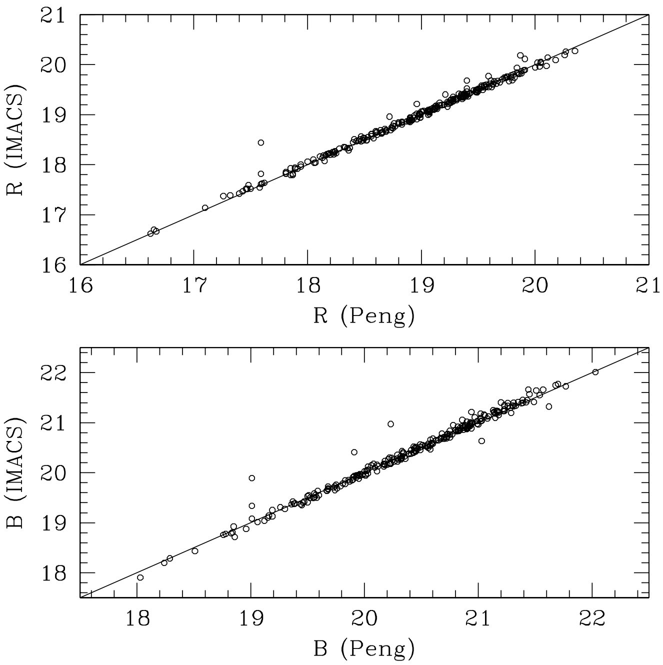

Figure 7. Final calibrated magnitudes for previously known globular clusters in NGC 5128, plotted against measurements for the same clusters by Peng et al. (2004b).

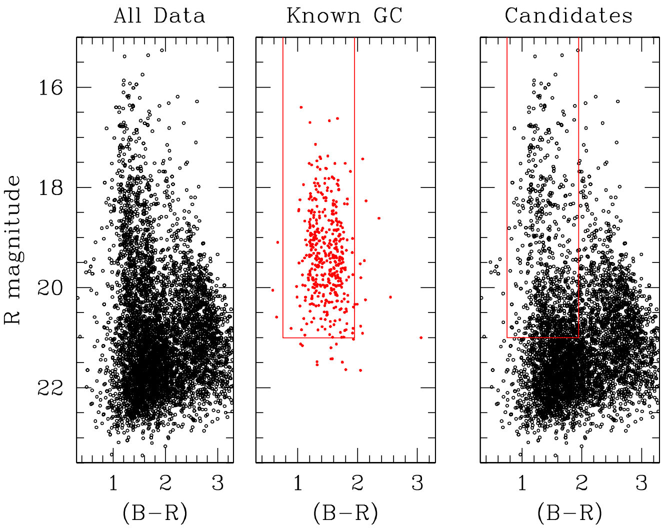

Figure 8. Left panel: color–magnitude diagram for all objects measured in the present study. These include the nonstellar objects found on the R-band images as described in the text. Middle panel: magnitudes and colors for the previously known globular clusters that were recovered by the search procedure. The marked box denotes the zone used for selection of the "best" GC candidates. Right panel: magnitudes and colors for the objects not previously known to be GCs. The 833 lying within the box are our final list of candidates.

(A color version of this figure is available in the online journal.)

measured in the *UBVRI* system, aperture corrected to large radius, and calibrated directly to Landolt (1992) standard stars. From the Peng et al. list 253 clusters were found overlapping our candidates. For these, mean offsets were calculated to bring the preliminary magnitudes into the final B, R scales. We found that the B magnitudes predicted from the Washington filters needed to be corrected by +0.08 and the R magnitudes by −0.07. Our fully corrected BR values for this calibrating list of clusters are shown in Figure 7. The residual scatter around the 1:1 line in each case is ±0.05 mag, which we take to be a fair indicator of the internal precision of the photometry in our final list.

3. FINAL SELECTION OF CANDIDATES

The candidates selected by the procedure described above consisted of 5411 objects that were (1) judged to be nonstellar, (2) not obviously background galaxies, and (3) measurable for photometry on both the B and R images. The second major stage in selection was to use magnitude and color.

The color–magnitude diagram for this entire candidate list is shown in Figure 8. Among these are the 458 rediscovered previous GCs, which are shown separately in the middle panel. The known clusters almost all fall within a well-defined part of the diagram, $0.95 \lesssim (B - R) \lesssim 1.95$. The well-known classic bimodal distribution of GC colors can be seen with the "blue" metal-poor clusters near $(B - R) \simeq 1.3$ and the "red" metal-rich ones near $(B - R) \simeq 1.6$. At the faint end, field contamination unfortunately becomes overwhelmingly large for $R \gtrsim 21$, and for these very low luminosity levels, higher-resolution imaging data than the current material will be needed to select out GCs efficiently from the background of very small, faint galaxies that dominate the population there

In Figure 8(b) showing previously cataloged GCs, about a dozen objects scatter to the red of the main GC distribution (i.e., with $(B - R) > 1.95$), raising the possibility that they are background objects that have been misclassified. These were closely inspected again on our images. Of these, one (GC 0066) is partially contaminated by the bleeding trail of a bright star. Five others (GC 0123, 0288, 0408, 0552, 0602) are possibly the bulges of faint galaxies based on their elliptical shape, diffuseness, and proximity to other galaxies in the field. The remainder showed no anomalies. New higher-precision velocity measurements will be needed to check the imaging analysis.

As a compromise between completeness and effective rejection of contaminants, we adopt the boundaries $R < 21$, $0.75 < (B - R) < 1.95$ to select out the best GC candidates. These are the 833 objects within the marked box in the right panel of Figure 8. Their distribution on the sky is shown in Figure 9, which for comparison also displays the 458 previously known GCs. As another comparison, Figure 10 shows the same new candidates along with the previously known GCs that were *not* identified by our current process.

Across the entire field, foreground reddening differs from place to place by ±0.03 mag in E_{B-V} (see, for example, http://irsa.ipac.caltech.edu/applications/DUST/). However, this amount of scatter is already smaller than our photometric precision in the measured GC colors (see above). In addition, this scatter is very much smaller than the intrinsic ∼±0.2 mag range in GC colors within both the blue (metal-poor) and red (metal-rich) sequences (8). Our cutoffs in color for candidate selection are therefore unaffected by realistic reddening differences.

Inspection of these two (α, δ) figures shows that the new candidates in some locations of the field form clumps or strings of points, which are likely to arise from background groups of galaxies, some of which are small and round with intermediate color and thus successfully masquerade as GC candidates despite our best efforts at classification. Two such strings of points are particularly noticeable at lower right. We inspected these regions again on the original images and verify that each marked point does belong to a real object that satisfies our classification criteria. The entire string is most probably a very distant background supercluster.

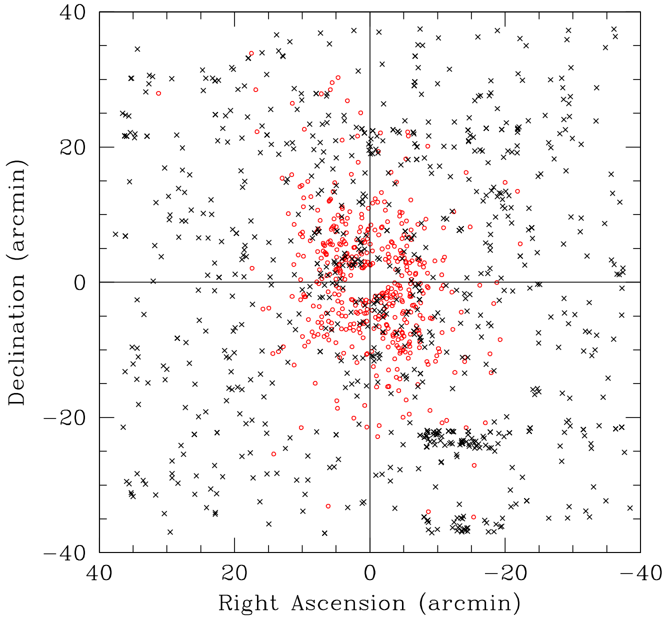

Figure 9. Location of the new GC candidates (black crosses) and the previously known GCs that were recovered in the search (red circles). The scales are in arcminutes relative to the center of NGC 5128, with east to the left and north to the top.

(A color version of this figure is available in the online journal.)

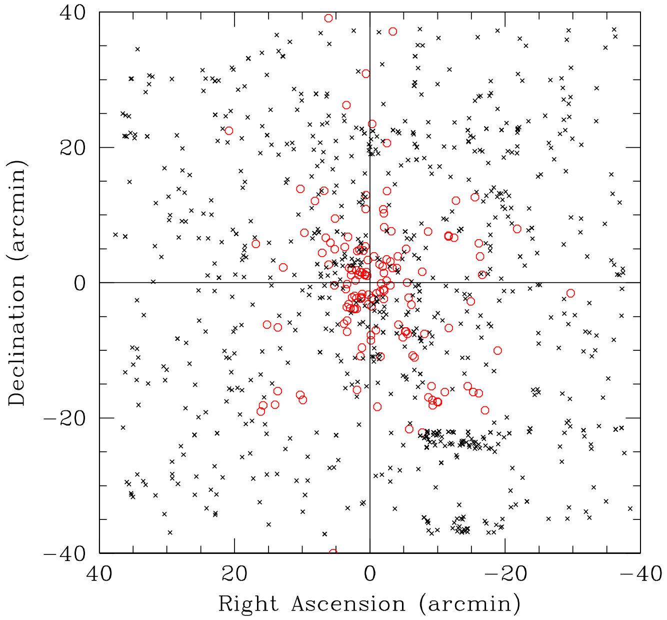

Figure 10. Location of the previously known GCs that were *not* recovered by the search procedure (red circles). As in the previous figure, small black crosses show the new GC candidates.

(A color version of this figure is available in the online journal.)

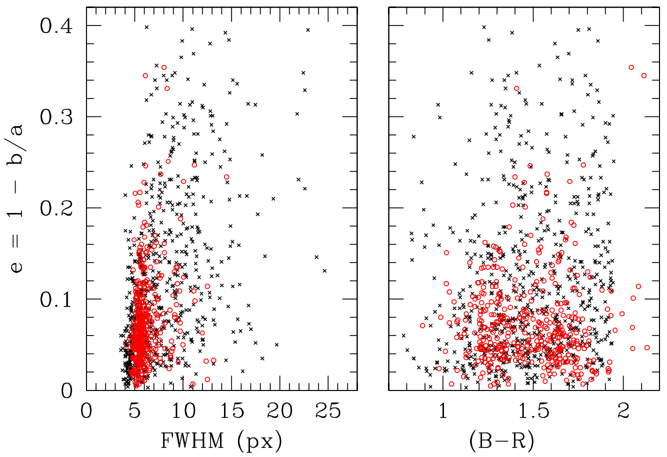

Figure 11. Left panel: ellipticity $e = (1 - b/a)$ plotted against FWHM for both the new cluster candidates (black crosses) and previously known clusters (red circles). Both parameters are measured from SourceExtractor. Right panel: ellipticity plotted vs. object color $(B - R)$ for the same objects.

(A color version of this figure is available in the online journal.)

As a final classification step we investigated the SourceExtractor parameters of ellipticity $e = 1 - b/a$ and scale size $fwhm$. Once again, we use the known GCs as a template to set appropriate ranges for these parameters. Plots of e versus $fwhm$ and $(B - R)$ are displayed in Figure 11. Normal GCs are quite round in projected profile, and the empirical data show that the great majority have $e < 0.2$ with only a small fraction in the larger range $0.2 < e < 0.4$. The majority also have sizes in the range $fwhm \simeq 5$–7 pixel, with the minimum around 4 pixel set by the seeing PSF (left panel of Figure 11). A few are found scattering up to $fwhm \sim 15$ pixel (1.″7 or 30 pc). These are similar to the largest known GCs in the Milky Way such as NGC 2419 or the Palomar-type halo clusters (Harris 1996).

The majority of the new objects selected by morphology, color, and magnitude are concentrated in the same $(e, fwhm)$ ranges as the known GCs, supporting their candidate classification. To avoid arbitrarily restricting our sample to too familiar a range of properties, however, we adopt rather generous cutoffs of $e < 0.4$ and $fwhm < 25$ pixel. These ranges include all the known clusters and allow for more unusual objects such as ultra-compact dwarfs) or extended clusters, which can have effective radii of 20–30 pc or more (e.g., Huxor et al. 2005; Evstigneeva et al. 2008). Future spectroscopic programs will be able to make definitive identifications.

The data for our final list of 833 new GC candidates, none of which are previously identified as clusters, are summarized in Table 1. Successive columns list (1,2) right ascension and declination in degrees; (3,4,5) B, R, and $(B - R)$; (6,7,8) location relative to the galaxy center $\Delta\alpha$, $\Delta\delta$, and projected galactocentric distance $R_{\rm gc}$, all with units of arcminutes; and (9,10) SE parameters e and $fwhm$.

Our present data use only two colors (B and R) and thus it is worth asking whether the addition of more color indices would significantly help weed out contaminants. For example, Rhode & Zepf (2001, see also the later papers in their series) used *BVR* photometry to help select GC candidates around several large galaxies including NGC 891, 3379, 4013, 4406, 4472, 4594, and 7814.

Extra color indices are not a perfect solution for removal of *stars*, because GCs fall along a part of the normal stellar two-color sequences (see particularly Figure 3 in Harris et al. 2004b for a good recent example using the CMT_1 system applied to NGC 5128). Fortunately, the high spatial resolution of our NGC 5128 field means that we have a much more powerful tool to remove the foreground-star contamination; that is, we have already removed almost all the stars by sample culling on the basis of size (FWHM) and morphology. As described above, we can then use magnitude, ellipticity, and a single color index $(B - R)$ to reduce the measured sample from ∼5400 candidates down to 833, an 85% culling fraction. Because some galaxies fall off the normal stellar/GC two-color sequence (see

Table 1
Globular Cluster Candidates in NGC 5128

α(J2000)	δ(J2000)	B	R	$B-R$	$\Delta\alpha'$	$\Delta\delta'$	$R'_{\rm gc}$	e	fwhm (pixel)
200.5075531	−43.4389915	20.787	19.155	1.632	−37.614	−25.189	45.270	0.026	5.610
200.5129700	−42.9849472	22.298	20.652	1.646	−37.377	2.053	37.433	0.186	6.880
200.5158081	−43.0344048	22.405	20.560	1.845	−37.253	−0.914	37.264	0.140	5.430
200.5169373	−43.3772964	22.188	20.797	1.391	−37.203	−21.488	42.962	0.245	7.660
200.5169373	−43.3772964	22.188	20.797	1.391	−37.203	−21.488	42.962	0.225	6.760

(This table is available in its entirety in machine-readable and Virtual Observatory (VO) forms in the online journal. A portion is shown here for guidance regarding its form and content.)

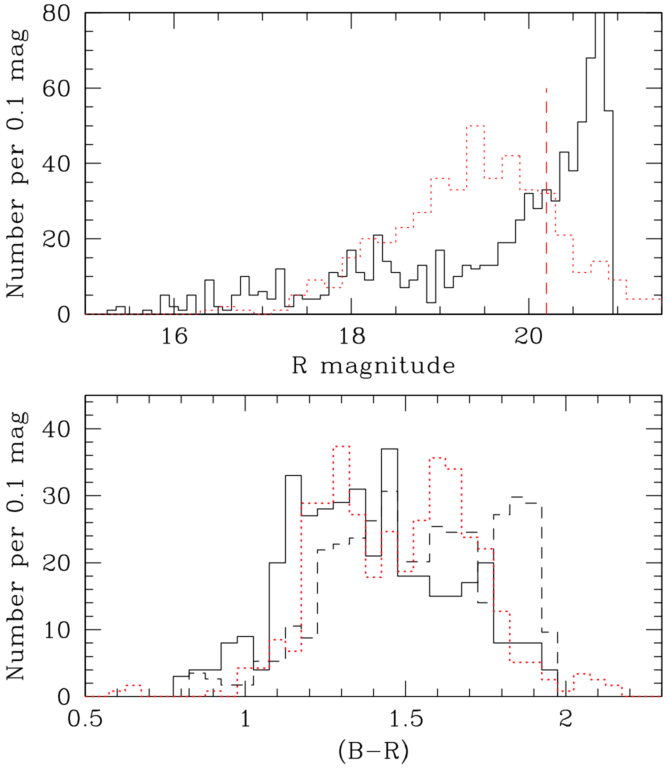

Figure 12. Upper panel: histogram of R magnitudes for the new GC candidates (black histogram) and for previously known GCs that were recovered in this study (red dotted histogram). The new candidates are strongly weighted toward the faint end. The vertical dashed line at $R = 20.2$ marks the expected luminosity of the GC luminosity function "turnover" or peak frequency. Lower panel: histogram of $(B-R)$ colors for the GC candidates brighter than $R = 20$ (black, solid line), the GC candidates with $20 < R < 21$ (dashed line), and the previously known clusters (dotted line). All three have been normalized to the same total number.

(A color version of this figure is available in the online journal.)

Rhode & Zepf 2001), the addition of a second color index might have incremental value in further trimming the sample. However, we believe the next major step (and subsequent scientific payoff) will come with spectroscopy and a velocity measurement program.

4. DISTRIBUTION FUNCTIONS

In Figure 12, the R magnitudes and $(B-R)$ colors of the new candidates are shown in histogram form, along with the same data for the previously known GCs. It is clear from the upper panel that the numbers of candidates increase strongly to the faint end of our data, suggesting increasing dominance of contaminants. However, the new candidate list promises to fill in the known cluster population brighter than the expected GC luminosity function "turnover point," which is at $R \simeq 20.2$.

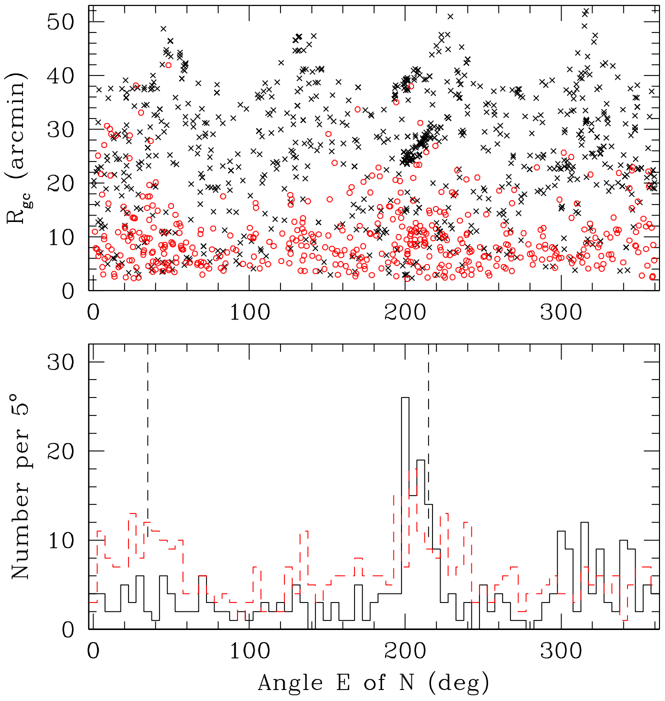

Figure 13. Upper panel: projected galactocentric distance $R_{\rm gc}$ vs. azimuthal angle θ (east of north). Black crosses denote the new candidates and red circles the 458 previously known clusters that were recovered in our study. Lower panel: histogram of position angle for both sets of objects, the candidates (solid line) and previously known clusters (dashed line). Here, only the candidates brighter than $R = 20$ and within radii $R_{\rm gc} < 36'$ are shown to minimize field contamination and exclude the objects near the corners. The two vertical dashed lines mark the position of the isophotal major axis of the halo.

(A color version of this figure is available in the online journal.)

For the color histogram (lower panel) we plot separately the 389 brighter candidates ($R < 20$, solid line) and the 444 fainter ones ($20 < R < 21$, dashed line). Within the adopted color boundaries (Figure 8), the brighter candidates show traces of the classic GC bimodal distribution, though with a much weaker red sequence than the known GCs. The relative lack of red GCs is to be expected, because the redder ones are already known to be more centrally concentrated around the galaxy (e.g., Harris et al. 2004b; Woodley et al. 2010b). By contrast, the fainter group of candidates is weighted more strongly to the red, indicating again the likely presence of residual contamination.

The azimuthal and radial distributions are shown in Figures 13 and 14. The previously known GCs are predominantly within projected radii $R_{\rm gc} \lesssim 15'$ (17 kpc), and also show noticeable

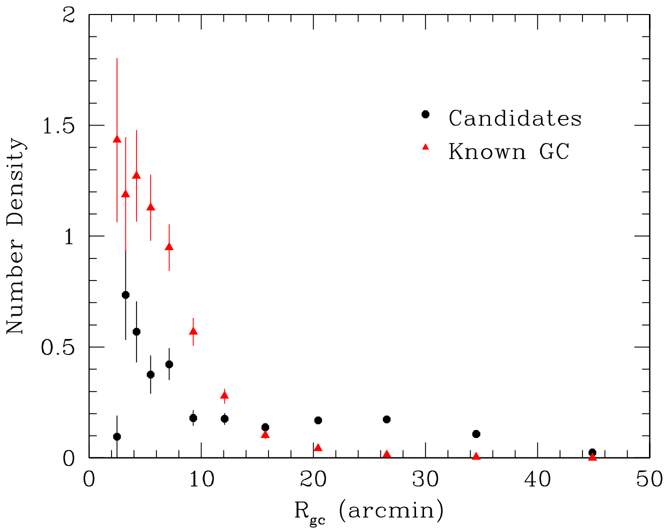

Figure 14. Projected number density (objects per arcmin^2) as a function of galactocentric distance $R_{\rm gc}$. As in previous figures, the new cluster candidates are in the black open symbols while the previously known GCs are in red.

(A color version of this figure is available in the online journal.)

concentration toward the isophotal major axis at $\theta = 35^\circ/215^\circ$ (Dufour et al. 1979). The relative lack of confirmed clusters out along the minor axis has been a longstanding concern, and it is simply not yet clear whether this is due to biases in previous surveys that have emphasized fields along the major axis or represents a true elongation of the GC system along with the rest of the galaxy halo. Our new IMACS list now gives complete azimuthal coverage out to $R_{\rm gc} \simeq 40$ kpc and should be capable of settling this question once follow-up spectroscopy can be done. Inspection of Figure 13 (lower panel) already indicates that the new candidate list is noticeably more uniformly distributed in θ than are the previously known GCs, consistent with the suspicion that many GCs remain to be found in the minor-axis directions. Our study has no selection effects by position angle θ that we are aware of, except for the innermost region around the dust lane. The previously mentioned clumps of points at $\theta = 200^\circ$–220° and $R_{\rm gc} = 30'$–$40'$ show up very obviously also in the "spike" of the histogram in Figure 13.

Lastly, the radial distribution (Figure 14) indicates that within $R_{\rm gc} \simeq 4'$, both the candidates and the re-identified known GCs are highly incomplete because of the very much brighter background light and interference from the dust lanes. Beyond this troublesome inner zone, we suggest that many dozens of good candidates lie within $4'$–$12'$; the success rate for spectroscopic follow-up should be high there. At larger radii the mean density of the candidates becomes rather flat, even ignoring the major "clumps" of candidates that create the gentle rise in the curve from $20'$ to $40'$. The sample contamination by field objects will be higher at these large radii, but any clusters successfully found there will carry high weight for the dynamic solutions and halo mass profile.

5. SUMMARY

We have carried out a new optical survey for GCs around NGC 5128, the nearby giant E galaxy. This study, built on B, R imaging with the Magellan IMACS camera, for the first time combines the benefits of wide-field coverage (1.4 deg^2) with excellent seeing quality ($0\farcs4$–$0\farcs5$). Selection of candidate objects was made by a combination of nonstellar shape, color, magnitude, and ellipticity. The result is a final list of 833 new GC candidates brighter than $R = 21$ and with astrometric positions better than $0\farcs2$ precision in each coordinate. We also independently re-identified 458 of the 607 previously known GCs.

We stress here once again the high potential astrophysical value of studying the NGC 5128 GC system in detail, which justifies new efforts to find many additional GCs. At present only a handful of GC systems can be as well studied to spectroscopic limits fainter than the GCLF turnover, and none of these others is a giant E galaxy.

This candidate list can be used as the basis for spectroscopic follow-up, velocity measurement, and a more comprehensive kinematic and dynamic study of the halo. Lingering concerns about spatial biasses in the known GCs that have afflicted earlier studies should now be removable to much larger distances into the halo. We are currently planning new spectroscopic observations for velocity measurement.

The high quality of the IMACS imaging already allows measurements of the structural parameters of the clusters (effective radii and central concentrations) for a much more comprehensive sample than before. Preliminary reports on the cluster parameters are given by Gómez & Woodley (2007) and Woodley & Gómez (2010) and a more extensive analysis is in progress.

We are grateful to Brian Schmidt for guiding the astrometric solutions which considerably helped the data reduction process. G.L.H.H. and W.E.H. acknowledge NSERC (Natural Sciences and Engineering Research Council of Canada) for financial support. D.G. gratefully acknowledges support from the Chilean projects *Centro de Astrofísica* FONDAP No. 15010003 and the Chilean Centro de Excelencia en Astrofísica y Tecnologías Afines (CATA) BASAL PFB/06. The superior quality of the IMACS camera and the exceptional seeing at the Magellan telescope were crucial for the success of this program. Finally, we also acknowledge with pleasure the staff and support at Mount Stromlo Observatory, where the various pieces of this work could finally come together.

REFERENCES

Ashman, K. M., & Zepf, S. E. 1998, Globular Cluster Systems (Cambridge: Cambridge Univ. Press)
Beasley, M. A., Bridges, T., Peng, E. W., et al. 2008, MNRAS, 386, 1443
Bertin, E., & Arnouts, S. 1996, A&AS, 117, 393
Brodie, J. P., & Strader, J. 2006, ARA&A, 44, 193
Calabretta, M. R., & Greisen, E. W. 2002, A&A, 395, 1077
Dufour, R. J., Harvel, C. A., Martins, D. M., et al. 1979, AJ, 84, 284
Evstigneeva, E. A., Drinkwater, M. J., Peng, C. Y., et al. 2008, AJ, 136, 461
Geisler, D. 1996, AJ, 111, 480
Gómez, M., Geisler, D., Harris, W. E., et al. 2006, A&A, 447, 877
Gómez, M., & Woodley, K. A. 2007, ApJ, 670, 105
Graham, J. A., & Phillips, M. M. 1980, ApJ, 239, L97
Harris, G. L. H. 2010a, PASA, 27, 475
Harris, G. L. H., Geisler, D., Harris, H. C., & Hesser, J. E. 1992, AJ, 104, 613
Harris, G. L. H., Geisler, D., Harris, W. E., et al. 2004a, AJ, 128, 712
Harris, G. L. H., Harris, W. E., & Geisler, D. 2004b, AJ, 128, 723
Harris, G. L. H., Poole, G. B., & Harris, W. E. 1998, AJ, 116, 2866
Harris, G. L. H., Rejkuba, M., & Harris, W. E. 2010a, PASA, 27, 457
Harris, W. E. 1991, ARA&A, 29, 543
Harris, W. E. 1996, AJ, 112, 1487
Harris, W. E. 2009, ApJ, 699, 254
Harris, W. E. 2010b, Phil. Trans. R. Soc., 368, 889
Harris, W. E., Harris, G. L. H., Barmby, P., McLaughlin, D. E., & Forbes, D. A. 2006, AJ, 132, 2187
Harris, W. E., Harris, G. L. H., Holland, S. T., & McLaughlin, D. E. 2002, AJ, 124, 1435

Harris, W. E., Kavelaars, J. J., Hanes, D. A., Pritchet, C. J., & Baum, W. A. 2009, AJ, 137, 3314
Harris, W. E., Spitler, L. R., Forbes, D. A., & Bailin, J. 2010b, MNRAS, 401, 1965
Hesser, J. E., Harris, H. C., & Harris, G. L. H. 1986, ApJ, 303, L51
Hesser, J. E., Harris, H. C., van den Bergh, S., & Harris, G. L. H. 1984, ApJ, 276, 491
Holland, S., Côté, P., & Hesser, J. E. 1999, A&A, 348, 418
Huxor, A. P., Tanvir, N. R., Irwin, M. J., et al. 2005, MNRAS, 360, 1007
Landolt, A. U. 1992, AJ, 104, 340
Lang, D., Hogg, D. W., Mierle, K., Blanton, M., & Roweis, S. 2010, AJ, 139, 1782
Larsen, S. S. 1999, A&AS, 139, 393
Monet, D. G., Levine, S. E., Canzian, B., et al. 2003, AJ, 125, 984
Mouhcine, M., Harris, W. E., Ibata, R., & Rejkuba, M. 2010, MNRAS, 404, 1157
Peng, E. W., Ford, H. C., & Freeman, K. C. 2004a, ApJ, 602, 705
Peng, E. W., Ford, H. C., & Freeman, K. C. 2004b, ApJS, 150, 367
Rejkuba, M., Minniti, D., Silva, D. R., & Bedding, T. R. 2001, A&A, 379, 781
Rhode, K. L., & Zepf, S. E. 2001, AJ, 121, 210
van den Bergh, S., Hesser, J. E., & Harris, G. L. H. 1981, AJ, 86, 24
Woodley, K. A., & Gómez, M. 2010, PASA, 27, 379
Woodley, K. A., Gómez, M., Harris, W. E., et al. 2010a, AJ, 139, 1871
Woodley, K. A., & Harris, W. E. 2011, AJ, 141, 27
Woodley, K. A., Harris, W. E., Beasley, M. A., et al. 2007, AJ, 134, 494
Woodley, K. A., Harris, W. E., & Harris, G. L. H. 2005, AJ, 129, 2654
Woodley, K. A., Harris, W. E., Puzia, T. H., et al. 2010b, ApJ, 708, 1335